LAWRENCE
LIVERMORE
NATIONAL
LABORATORY

LLNL-JRNL-831238

Emission lines of Fe XIV, Fe XV, and Fe XVI in the extreme ultraviolet region, 40 - 100 A

J. K. Lepson, P. Beiersdorfer, G. V. Brown, D. A. Liedahl

January 28, 2022

Astrophysical Journal

Disclaimer

Emission lines of Fe XIV, Fe XV, and Fe XVI in the extreme ultraviolet region 40 – 100 Å

J. K. Lepson, P. Beiersdorfer

Space Sciences Laboratory, University of California, Berkeley, CA 94720 USA

lepson@berkeley.edu

G. V. Brown, D. A. Liedahl

Physics Division, Lawrence Livermore National Laboratory, Livermore, CA 94550 USA

ABSTRACT

We report on emission spectra of iron in the extreme ultraviolet recorded at an electron density of $\sim 10^{11}\mathrm{cm}^{-3}$ on the Lawrence Livermore electron beam ion trap facility. We present a summary of the observed emission lines, including wavelengths and emission intensities, and present spectra of pure Fe XIV through Fe XVI emission derived from our measurements in the 40 – 100 Å wavelength range. We show that spectral models, especially the current version of CHIANTI v10.0, describe the M-shell emission from these three charge states of iron reasonably well, and we are able to verify several transitions in CHIANTI for the first time.

Subject headings: line: identification–methods: laboratory, analytical–sun: corona

1. Introduction

Accurate and complete spectral models are essential for the analyses of spectral emission data returned by current and former X-ray and extreme ultraviolet (hereafter referred to as EUV) missions, such as *EUVE*, the *Chandra X-ray Observatory*, *XMM−Newton*, *CHIPS*, and *Hinode*. Early on, deficiencies in available data sets have hampered analyses and have resulted in incorrect, incomplete, or contradictory interpretations of spectral observations (e.g. Jordan 1968, 1995; Mewe et al. 1995b; Stern et al. 1995; Schmitt et al. 1996a, 1996b). For example, a measurement of Fe IX and Fe X transitions at the Lawrence Livermore National Laboratory's EBIT-II electron beam ion trap in the 60 – 100 Å wavelength region showed that roughly 80% of the observed emission was not accounted for in global fitting

models at the time (Beiersdorfer et al. 1999b, Lepson et al. 2002). To a lesser extent, this was also true for Fe VII and Fe VIII. It was found that there was a high density of weak lines in the EUV spectral range from these charge states, forming a quasi-continuum that mimicked a high-temperature bremsstrahlung continuum (Beiersdorfer et al. 1999b). Although much progress has been made in compiling both measured and calculated EUV emission lines from astrophysically relevant ions (e.g., Lepson et al. 2003, 2005a, 2005b; Liang et al. 2009; Dere et al. 1997, 2019; Landi et al. 2006; Gu 2011; Beiersdorfer & Lepson 2012; Träbert et al. 2013, Beiersdorfer et al. 2014b; Träbert & Beiersdorfer 2018), data in the EUV region are still needed for many ions. This was reiterated in analyses of *Chandra* observations of Procyon and other cool stars (Beiersdorfer et al. 2014a, 2015), as well as *Hinode* observations of the Sun (Del Zanna & Mason 2018, Del Zanna et al. 2019).

Data from intermediate charge states of iron have received renewed interest since the launch of the *Solar Dynamics Observatory* (SDO) (Boerner et al. 2012, Lemen et al. 2012). SDO's Atmospheric Imaging Assembly (AIA) monitors the iron emission in six spectral bands centered on various prominent iron lines. Large sets of laboratory data from various astrophysically relevent ions have been collected to aid the spectral modelling effort of the AIA channels (Träbert et al. 2014a, 2014b, 2016, 2018a; Beiersdorfer et al. 2014b, 2018). One of these bands covers the region near 94 Å, which includes not only emission from Fe XVIII but also from Fe X. Our earlier studies of the Fe VII – Fe X (Lepson et al. 2002) already showed that there are additional lines in this AIA bandpass from Fe IX that need to be taken into account when modeling the response of this channel, as discussed by Testa, Drake, & Landi (2012). The search for additional iron lines that are not yet modeled but may be relevant for understanding the response of the AIA channels continues to be a high priority.

In the following we present a detailed line list of Fe XIV, Fe XV, and Fe XVI spectra obtained at the Lawrence Livermore electron beam ion trap (EBIT) facility in the 40 – 100 Å range. Although our measurements extend beyond 150 Å, we were unable to verify any iron features above ∼100 Å; any lines there are too weak to be confidently identified. Indeed, a high-resolution measurement of iron lines near the AIA 131 Å channel did not uncover any Fe XIV - Fe XVI lines in their region of interest (Träbert et al. 2014a). We measured wavelengths of individual features observed in the spectra with an accuracy of 0.02 Å and present relative intensities of these features. We have correlated our results with predictions from published line lists, and we present new calculations to complement our measurements. The result is a comprehensive listing of the spectral features in the Fe XIV, Fe XV, and Fe XVI spectra between 40 and 100 Å, including wavelengths, relative intensities, and identifications, as pertinent to the plasma conditions of our laboratory measurements.

These line lists provide new lines necessary to complete models employed in global fits. It may also aid in the identification of some of the stronger Fe XIV, Fe XV, or Fe XVI lines in iron-rich cool stars such as the Sun, α-Cen, Procyon, 44i-Boo, and AU-Mic.

2. Laboratory methods and measurements

The Lawrence Livermore National Laboratory's EBIT facility, which was used to make the present measurements, is the longest running of its kind, and has been optimized for laboratory astrophysics measurements (Beiersdorfer 2003). The facility is well suited for the present investigations because it can be operated at the relatively low voltages (400-500 eV) necessary to produce the charge states we investigated (Lepson & Beiersdorfer 2005). Moreover, different charge states can be produced simply by changing the voltage of the electron beam. When the voltage increases, higher charge states appear as the ionization potential is exceeded, and lower charge states decline and disappear as they "burn out." Ideally, charge states appear one by one as the voltage increases. In practice, however, there is some mixing present because of recombination. In addition, the next higher state is sometimes present because of a $\sim$30 eV spread in the beam energy, which is comparable to the separation in ionization potentials in the region of interest. The typical spectrum thus contains 1 – 3 charge states in addition to the dominant one. By systematically recording spectra at different energies, however, it is possible to isolate the emission of a single charge state (Lepson et al. 2000, 2002).

Spectra were measured with a grazing-incidence spectrometer described by Beiersdorfer et al. (1999a) employing an average 1,200 line/mm flat-field grating developed by Harada and Kita (1980; Nakano et al. 1984) with a 3° angle of incidence. Similar instruments from LLNL have also been installed at the National Spherical Torus Experiment (Graf et al. 2008, Lepson et al. 2010, Weller et al. 2016), the Alcator C-Mod tokamak (Reinke et al. 2010, Lepson et al. 2012), and the DIII-D tokamak (Victor et al. 2017). Readouts were taken with a back-illuminated, liquid nitrogen-cooled CCD camera with a one inch square array of 1,024 $\times$ 1,024 pixels and a resolving power, E/ΔE, of $\sim$300 at 100 Å. A typical exposure, or "run" lasted 30 minutes.

Spectra were calibrated using the well known K-shell emission lines of nitrogen, in particular the N VII Lyman-α line and the N VI resonance line commonly referred to as w, as described by Beiersdorfer et al. (1999a). These lines were observed in 1st through 7th order, which provided an accurately calibrated region from 25 - 190 Å. Calibration spectra were taken periodically throughout the experimental run.

Spectra were also taken without an active trap, i.e., without a potential applied to the trap electrodes, as described earlier (Lepson et al. 2002, Chen et al. 2004). These spectra enabled us to determine the level of background emission (including visible light from the electron-gun filament, to which the CCD camera is sensitive), which was then subtracted from the iron spectra to yield background-corrected spectra. Background spectra were typically taken after every few Fe spectra to ensure maximum accuracy in assessing the true iron emission levels. As part of the image processing, we also filtered out strong stray cosmic rays from the spectra in order to avoid any "false" peaks.

The electron density of the electron cloud in our measurements is about $1-2\times10^{11}cm^{-3}$, which is comparable to the densities of many astrophysical plasmas. This is near the upper range of such measurements on our device (Chen et al. 2004, Arthanayaka et al. 2020), as we have aimed to obtain the best signal to noise ratio by maximizing the number of trapped iron ions and their interaction with the electron beam.

Figure 1 shows background subtracted spectra obtained at beam energies of 360, 420, and 550 eV. The dominant charge states are Fe XIV, Fe XV, and Fe XVI, respectively, in accordance with their ionization potentials of 392, 457, 489 eV, respectively. Note that lower charge states, down to Fe XII, are also present in the spectra.

Ideally, we would like to record only spectra from a single charge state in order to facilitate identification of emission lines. Given the large number of lines, attribution of any particular feature to the emitting ion can be difficult in spectra that contain more than one charge state. But because we have recorded spectra at different electron beam energies with different dominant charge states, we are able to isolate the emission from a single charge state by proper subtraction of spectra taken at lower and higher beam energies, which are dominated by lower and higher charge states, respectively. This was done following the procedure detailed by Lepson et al. (2000, 2001). We present the resulting "pure" Fe XIV, Fe XV, and Fe XVI spectra in Figs. 2 through 4.

We note that the subtraction procedure introduces a certain amount of statistical noise into the resulting spectrum, which can hinder the identification of very weak lines. However, identification of weak lines is aided by analyzing multiple runs. While the increased noise level is clearly undesirable, the advantage of the subtraction procedure is that a pure spectrum from a single charge state is produced for comparison with calculations and easier line identification. Fortunately, the iron charge states of interest to our work produce comparatively simple spectra (compared to many other charge states of iron), and the "pure" spectra resulting from the subtractions have relatively little noise.

Peaks were fitted with Gaussian trial functions employing the program IGOR (www.wavemetrics.com)

to determine line positions and relative intensities, using the original spectra, such as those shown in Fig. 1. A summary of the results is given in Tables 1 – 3. Moreover, the measured wavelengths are annotated to the lines in Figs. 2, 3, and 4. Errors in the wavelength were computed as standard errors determined from line positions fitted in separate runs. Spectra from up to 15 runs were fitted to obtain the wavelengths of the lines in a given charge state. In some cases, as noted in the tables, we used the second order spectrum to determine wavelengths of closely separated features, but in all cases the line intensities were measured using the first order spectrum.

The measured line intensities given in Tables 1 – 3 were corrected for the responsivity function of the spectrometer. Here we relied on a calibration of the spectrometer performed at the Lawrence Berkeley National Laboratory's Advanced Light Source (Lepson et al. 2001, May et al. 2003). The response function peaks at 80 Å, dropping to near 10% at 40 Å and 200 Å. Unlike the entries in the tables, the spectra shown in Figs. 2 – 4 have not been corrected for the response function. This was done for the interest of clarity as the noise in those regions is also amplified and makes the figure extremely unsightly. Therefore, the actual intensities of lines at the high and especially the low end of the region studied are greater than indicated by the figures.

Where identification was possible, we have listed in Tables 1 – 3 the transition associated with a given feature. Line identification was enabled in part by comparison with the MEKAL line list (Mewe et al. 1995), which has now been incorporated into the spectral X-ray modeling package SPEX v3.0 (Kaastra et al. 1996), as well as the line list provided by Kelly (1987). The wavelengths from these line lists are listed in Tables 1 - 3 for comparison. Because these line lists mainly utilize measured values from prior observations or experiments for the lines of interest here, the wavelength values are very similar.

In addition, line identification was enabled by comparison with the spectral data provided by the CHIANTI v10.0 database (Del Zanna et al. 2021) as well as by our own calculations using the Hebrew University - Lawrence Livermore Atomic Code (HULLAC) (Bar-Shalom et al. 2001). The wavelengths from CHIANTI and our own calculations are also listed in Tables 1 – 3. Note that the CHIANTI database contains many, mostly weak, lines that are noted as only having theoretical energy levels and "not very accurate" wavelengths (Dere et al. 1997, Del Zanna et al. 2021). We have labeled these lines as "unverified" in the tables.

The spectral databases as well as our own HULLAC calculations provide line intensity information and can thus be used to construct synthetic spectra for comparison with our measurements. Moreover, these synthetic spectra can be used to investigate lines that are sensitive to density effects. This is discussed in detail in the following section, where we

show in Figs. 5 through 8 synthetic spectra from different models and compare them to the pure iron spectra from our measurements.

We note that AtomDB v3.0, which is an atomic database and spectral modeling code focused on X-ray astronomy (Foster et al. 2012), also gives a list of relevant iron lines. The entries for Fe XV and Fe XVI are identical to those in CHIANTI, and we do not list those separately in our tables. However, we discuss the the AtomDB entries for Fe XIV in the subsequent subsection, and we include the synthetic spectra based on AtomDB data for comparison with the measurements and the other synthetic spectra in Figs. 5, 6 and 7.

3. Discussion

In this section we discuss the spectra of iron by charge state. Our focus is on an assessment of the relative line intensities and whether all measured lines are included in the models.

The synthetic spectra show that the intensities of the Fe XIV lines are sensitive to the electron density between the zero-density limit and the densities encountered in our apparatus ($< 10^{12}$ cm^{-3}), and we include a discussion of this effect in the next subsection. By contrast, neither Fe XV nor Fe XVI show such a dependency.

3.1. Fe XIV

In Fig. 5(a) we show a synthetic spectrum based on data from AtomDB v3.0 (Foster et al. 2012), which was calculated in the zero-density limit, and three synthetic spectra constructed from the CHIANTI v10.0 database (Dere et al. 2019) at electron densities of (b) 10^6 cm^{-3}, (c) 10^{10} cm^{-3}, and (d) 10^{15} cm^{-3}. The relative intensities of the Fe XIV lines clearly change at each density, and, at the lowest two densities, some lines disappear completely while new ones appear.

At the higher densities near those to the experimental conditions, changes in the line intensities are not as significant. In fact, the spectra are essentially the same for densities between 10^{11} and 10^{12} cm^{-3}, which we explored with our HULLAC calculations. In Table 1 we list the intensities calculated with HULLAC at 5×10^{11} cm^{-3}, and we show the corresponding spectrum in Fig. 6 for comparison with the measured "pure" Fe XIV spectrum.

There are obvious similarities between the HULLAC spectrum and our data. However, there are also some glaring discrepancies. For example, the line pair predicted by HULLAC

to be at 82.5 Å is likely the feature measured just above 80 Å, which is a difference of more than +2 Å. Similarly, the line pair predicted by HULLAC to be at 91 Å is likely the feature measured above 93 Å, which is a difference in more than −2 Å. The lines we measure at 67.194 and 67.333 Å appear to be absent in our HULLAC calculations, unless they correspond to the lines predicted by HULLAC at 63.157 and 63.210 Å, which do not appear in the measured spectrum near this wavelength. If so, this would mean a wavelength discrepancy of −4 Å, i.e., twice of what we have established for some of the other lines. Because the line positions are uncertain and because many features comprise more than one line, it is also difficult to assess the quality of the calculated line intensities other than to say, that there is overall resemblance but the details do not readily match.

There is a distinct possibility that some of these discrepancies in the line intensities between the experimental data and HULLAC arise because line excitation in EBIT is by a monoenergetic electron beam rather than by the Maxwellian electron distribution function as assumed by the models. In the case of Fe IX, for example, we found that the lines from higher n levels (4 → 3 relative to 3 → 3) may be enhanced by a factor of 2–3 when excited by an electron beam relative to excitation by a Maxwellian plasma because more energetic lines are more readily excited (Lepson et al. 2002). In the case of Fe XIV, calculations using a monoenergetic beam changed the intensities of only a few lines, and by not more than 50%, whereby some lines appear to agree better with the data, but some others more poorly. In other words, the agreement to the measured data does not improve.

Because neither of the CHIANTI spectra calculated at 10^{10} or 10^{15} cm^{-3} provides a perfect match to our measured spectrum, we chose a CHIANTI spectrum at the intermediate density of 5×10^{12} cm^{-3} in Fig. 6. Unlike our HULLAC spectrum, the CHIANTI spectrum, however, provides a very good match. The wavelengths of the features shown in the CHIANTI spectrum line up very well with the positions in the experimental spectrum. For example, the line pair predicted by HULLAC to be at 82.5 Å is listed in CHIANTI to be just above 80 Å and, thus, agrees very well with the measurements of the lines at 80.142 and 80.453 Å. Similarly, the two lines we measure just above 67 Å and discussed in the previous paragraph is reproduced by CHIANTI within 0.1 Å. (N.B. that the upper and lower configurations do not match with those of the candidate lines in HULLAC near 63 Å.) In fact, even the lines listed in CHIANTI as "unverified" and shown dotted in Fig. 6(c) match very well with the positions of the measured features. This includes the predicted feature at 72.95 Å, which appears to be the feature measured at 72.731 Å, and the 4 → 3 features just above 55 Å, between 60 and 61 Å, and near and 76.7 Å. It also includes the feature at 88 Å, although in the latter case the wavelength difference between 88.103 Å (CHIANTI) and

88.937 Å (measured) is markedly larger than for other lines in CHIANTI.

Unlike for Fe XV and Fe XVI the line list in AtomDB v3.0 for Fe XIV is different from that in CHIANTI v10.0. In general the wavelengths in AtomDB are closer to the measured values than our HULLAC numbers, but they are not as close as the CHIANTI wavelengths. For example, CHIANTI lists 80.206 Å for the line we measure at 80.142 Å, while AtomDB gives 79.159 Å. Similarly, CHIANTI's line at 71.939 Å is given in AtomDB as 71.295 Å, while we measured it at 71.903 Å.

The current version of CHIANTI clearly does by far the most creditable job for Fe XIV. Its line list is more complete than that given by Kelly or in SPEX, and its wavelengths are the more accurate than those in AtomDB or those we calculated with HULLAC.

3.2. Fe XV

In Fig. 7 we show the comparison of various synthetic spectra with the measurements for Fe XV. The synthetic spectra were calculated at very different densities: HULLAC employing a density of 5×10^{11} cm^{-3}, CHIANTI 1×10^{10} cm^{-3}, and AtomDB the zero-density limit. The fact that there is no obvious variation in the line intensities illustrates that the Fe XV line emission is not effected by density effects.

Comparing the spectra in In Fig. 7 with our measurement we find that HULLAC includes essentially all lines with accurate positions and fairly accurate intensities in the region >60 Å. Like HULLAC, CHIANTI does a good job in including the features we observed, although it misses the same $5 \rightarrow 3$ transitions near 50 – 52 Å that appear to be missing from HULLAC. The feature around 83 Å is underpredicted nearly to the vanishing point by CHIANTI, while HULLAC gives this double feature much more flux, albeit not as much as measured. CHIANTI only has a single verified line at this wavelength, and at least one of the unverified lines are needed to produce the observed double-humped feature. The AtomDB spectrum essentially repeats the CHIANTI spectrum. Interestingly, the strongest feature in Fe XV, the 4s $\rightarrow$ 3p transition at 69.7 Å, appears to be over predicted by all models relative to the neighboring lines compared to our measurements.

3.3. Fe XVI

We show the comparison between our measurement and synthetic spectra for Fe XVI in Fig. 8. As before, the synthetic spectra were calculated at a density of 5×10^{11} cm^{-3} with HULLAC, at 1×10^{10} cm^{-3} with CHIANTI, and in the zero-density limit with AtomDB.

All three databases do a good job at reproducing the relatively simple spectrum of Fe XVI, including the relative intensities of the 4d → 3d line pair at 54.1 Å and 54.7 Å and the 4f → 3d line pair at 62.9 Å and 63.7 Å. The largest difference from our measurements is in the relative intensity of the latter line pair, which is roughly 40% stronger in all three models compared to the measured intensity of the neighboring lines. The one moderately strong line around 45 Å listed by CHIANTI as "unverified" (shown dotted in Fig. 8(c)) could not be confirmed by our measurements. Although all other CHIANTI lines are mirrored in AtomDB, this line (rightfully) is not. All three models include a few 5 → 3 transitions around 40 – 42 Å that were not observed in our measurements. Finally, the line we measured at 52.8 Å is absent from all the models. We recognize that the position of this feature is nearly identical to the 4d → 3d feature of Fe XV in Fig. 7. We note that the height of this line relative to Fe XV's strongest line is greater in Fig. 1(c) (taken at a beam energy of 550 eV) than in Fig. 1(b) (beam energy 420 eV), and we believe it is therefore an artifact resulting from that feature being under-subtracted when we removed the Fe XV emission from the raw Fe XVI spectrum.

4. Summary

We found that our measurements of M-shell iron emission from Fe XIV, Fe XV, and Fe XVI were reasonably well described by the HULLAC, AtomDB, and CHIANTI databases. In particular, CHIANTI v10.0 has made great strides since our earlier reports on Fe VII – Fe X (Lepson et al. 2002). We find that CHIANTI has a nearly complete line list and has the most accurate wavelengths of the databases to which we compared our measurements. We recommend the use of the CHIANTI wavelengths for those lines for which wavelengths are not available from previously measured or from our currently measured values. Most of the features we observed were found in all three models, although relative intensities typically varied, sometimes substantially, from what we measured. In addition, we were able to confirm a number of features listed by CHIANTI as "unverified". Although these models are a useful tool for identification, laboratory benchmarking is still necessary, particularly for the case of astrophysical plasmas in which several elements and/or charge states are present, as emission lines may blend together. This makes an accurate knowledge of the line position and relative line intensity essential for analysis.

This work was supported by grants 80NSSC20K0916 and NNH16AC82I from NASA's Solar and Heliospheric Physics Program and was performed in part under the auspices of the U.S. Department of Energy by Lawrence Livermore National Laboratory under Contract DE-AC52-07NA27344. This document was prepared as an account of work sponsored by an

REFERENCES

Arthanayaka, T., Beiersdorfer, P., Brown, G. V., Gu, M. F., Hahn, M., Hell, N., Lockard, T., & Savin, D. W. 2020, ApJ, 890, 77.

Bar-Shalom, A., Klapisch, M., & Oreg, J. 2001, J. Quant. Spectrosc. Rad. Transf., 71, 169.

Beiersdorfer, P. 2003, Ann. Rev. Astron. Astrophys., 41, 343.

Beiersdorfer, P. 2008, Can. J. Phys., 86, 1.

Beiersdorfer, P. & Lepson, J. K., 2012, ApJ Suppl., 201, 28.

Beiersdorfer, P., Crespo López-Urrutia, J. R., Springer, P., Utter, S. B., & Wong, K. L. 1999a, Rev. Sci. Instrum., 70, 276.

Beiersdorfer, P., Lepson, J. K., Brown, G. V., Utter, S. B., Kahn, S. M., Liedahl, D. A., & Mauche, C. W. 1999b, ApJ, 519, L185.

Beiersdorfer, P., Hell, N., Lepson, J. K., Díaz, F., & Ishikawa, Y. 2015, ApJ 815, 3.

Beiersdorfer, P., Lepson, J. K., Desai, P., Díaz, F., & Ishikawa, Y. 2014, ApJ Suppl., 210, 16.

Beiersdorfer, P., Träbert, E., Lepson, J. K., Brickhouse, N. S. & Golub, L. 2014, ApJ, 788, 25.

Beiersdorfer, P. & Träbert, E. 2018, ApJ, 854, 114.

Boerner, P., Edwards, C., Lemen, J., et al. 2012, Solar Phys., 275, 40.

Chen, H., Beiersdorfer, P., Heeter, L. A., Liedahl, D. A., Naranjo-Rivera, K. L., Träbert, E., Gu, M. F., & Lepson, J. K. 2004, ApJ, 611, 598.

Del Zanna, G., Dere, K. P., Young, P. R. & Landi, E. 2021, ApJ, 909, 38.

Del Zanna, G., Gupta, G. R. & Mason, H. E. 2019, A & A 631, 163

Del Zanna, G., & Mason, H. E. 2018, Living Rev. Sol. Phys., 15, 5.

Dere, K. P., Landi, E., Mason, H. E., Monsignori Fossi, B., & Young, P. R. 1997, A&AS, 125, 149.

Foster, A. R., Ji, L., Smith, R. K. & Brickhouse, N. S. 2012, ApJ, 756, 128.

Graf, A. T., Brockington, S. Horton, R., Howard, S., Hwang, D., Beiersdorfer, P., Clementson, J., Hill, D., May, M., McLean, H., Wood, R., Bitter, M., Terry, J., Rowan, W. L., Lepson, J. K., & Delgado-Aparicio, L. 2008, Can. J. Phys., 86, 307.

Gu, M. F., Beiersdorfer, P., & Lepson, J. K. 2011, ApJ, 732, 91.

Harada T. & Kita, T., 1980, Appl. Opt. 19, 3987.

Jordan, C., 1968, J. Phys. B, 1, 1004.

Jordan, C., 1995, Astrophysical Applications of Powerful New Databases. Joint Discussion No. 16 of the 22nd. General Assembly of the I.A.U., held in The Hague, Netherlands, August 22-23, 1994. ASP Conference Series, Volume 78. Editor(s), S.J. Adelman, W.L. Wiese; Publisher, Astronomical Society of the Pacific, San Francisco, California, 1995. LC : QB465 .A88 1994. ISBN : 0-937707-97-X., p.371

Kaastra, J. S., Mewe, R. & Nieuwenhuijzen, H. 1996, 11th Colloquium on UV and X-ray Spectroscopy of Astrophysical and Laboratory Plasmas, Editors, K. Yamshita, T. Watanabe; p. 411.

Kelly, R. L. 1987, J. Phys. Chem. Ref. Data Suppl., 16, 1.

Landi E., Del Zanna, G., Young, P. R., Dere, K. P., Mason, H. E., & Landini, M. 2006. ApJ Suppl., 162, S261.

Lemen, J. R., Title, A. M., Akin, D. J., et al., 2012, Solar Phys., 275, 15.

Lepson, J. K. & Beiersdorfer, P. 2005, Phys. Scripta, T120, 62.

Lepson, J. K., Beiersdorfer, P., Brown, G. V., Chen, H., Gullikson, E. M., Schneider, M. B., Utter, S. B., & Wong, K. L. 2001, University of California Lawrence Livermore National Laboratory Report UCRL-ID-142264 [available at http://www.llnl.gov/tid/Library.html].

Lepson, J. K., Beiersdorfer, P., Brown, G. V., Kahn, S. M., Liedahl, D. A., Mauche, C. W., & Utter, S. B. 2000, Rev. Mexicana Astron. Astrofis. Ser. de Conf., 9, 137.

Lepson, J. K., Beiersdorfer, P., Brown, G. V., Liedahl, D. A., Utter, S. B., Brickhouse, N. S., Dupree, A. K., Kaastra, J. S., Mewe, R.,& Kahn, S. M. 2002, ApJ, 578, 648.

Lepson, J. K., Beiersdorfer, P., Behar, E., & Kahn, S. M. 2003, ApJ, 590, 604.

Lepson, J. K., Beiersdorfer, P., Behar, E., & Kahn, S. M. 2005, ApJ, 625, 1045.

Lepson, J. K., Beiersdorfer, P., Behar, E., & Kahn, S. M. 2005, Nucl. Instrum. Methods B, 235, 131.

Lepson, J. K., Beiersdorfer, P., Clementson, J. Gu, M. F. Bitter, M. Roquemore, L. Kaita, R., Cox, P. G., & Safronova, A. S. 2010, J. Phys. B, 43, 14401.

Lepson, J. K., Beiersdorfer, P., Gu, M. F., Desai, P., Bitter, M., Roquemore, L., Reinke, M. L. 2012, AIP Conf. Proc., 1438, 136.

Liang, G. Y., Baumann, T. M., Crespo López-Urrutia, J. R., et al., 2009, ApJ, 696, 2275.

May, M., Lepson, J., Beiersdorfer, P., Thorn, D., Chen, H., Hey, D., & Smith, A. 2003, Rev. Sci. Instrum., 74, 2011.

Mewe, R., Kaastra, J. S., & Liedahl, D. A. 1995, Legacy, 6, 16.

Mewe, R., Kaastra, J. S., Schrijver, C. J., van den Oord, G. H. J. & Alkemade, F. J. M. 1995, A&A, 296, 477.

Reinke, M. L., Beiersdorfer, P. Howard, N. T., Magee, E. W., Podpaly, Y., Rice, J. E. Terry, J. L. 2010, Rev. Sci. Instrum. 81, 10D736.

Schmitt, J. H. M. M., Stern, R. A., Drake, J. J., Kuerster, M. 1996, ApJ, 464, 898.

Schmitt, J. H. M. M., Drake, J. J., Stern, R. A. 1996, ApJ, 465, L51.

Stern, R. A., Lemen, J. R., Schmitt, J. H. M. M. & Pye, J. P. 1995, ApJ. 444, L45

Testa, P., Drake, J. J., Landi, E. 2012, ApJ, 745, 111.

377 Träbert, E., & Beiersdorfer, P. 2013, Phys. Scr., 156, 014003.

378 Träbert, E., & Beiersdorfer, P. 2015, J. Phys. C, 583, 2008.

379 Träbert, E., & Beiersdorfer, P. 2018 A&A, 617, 8.

380 Träbert, E., Beiersdorfer, P., Brickhouse, N. S., & Golub, L. 2014a, ApJ, S211, 14.

381 Träbert, E., Beiersdorfer, P., Brickhouse, N. S., & Golub, L. 2014b, ApJ, S215, 6.

382 Träbert, E., Beiersdorfer, P., Brickhouse, N. S., & Golub, L. 2016, A&A 586, 115.

383 Träbert, E., Beiersdorfer, P., Lepson, J. K. Reinke, M. L., & Rice, J. E. 2018, ApJ, 865, 148

384 Victor, B. S., Allen, S. L., Beiersdorfer, P., & Magee, E. W. 2017, J. Instrum. 12, C06011.

385 Weller, M. E., Beiersdorfer, P., Soukhanovskii, V. A., Magee, E. W., & Scotti, F. 2016, Rev.
386 Sci. Instrum. 87, 11E384.

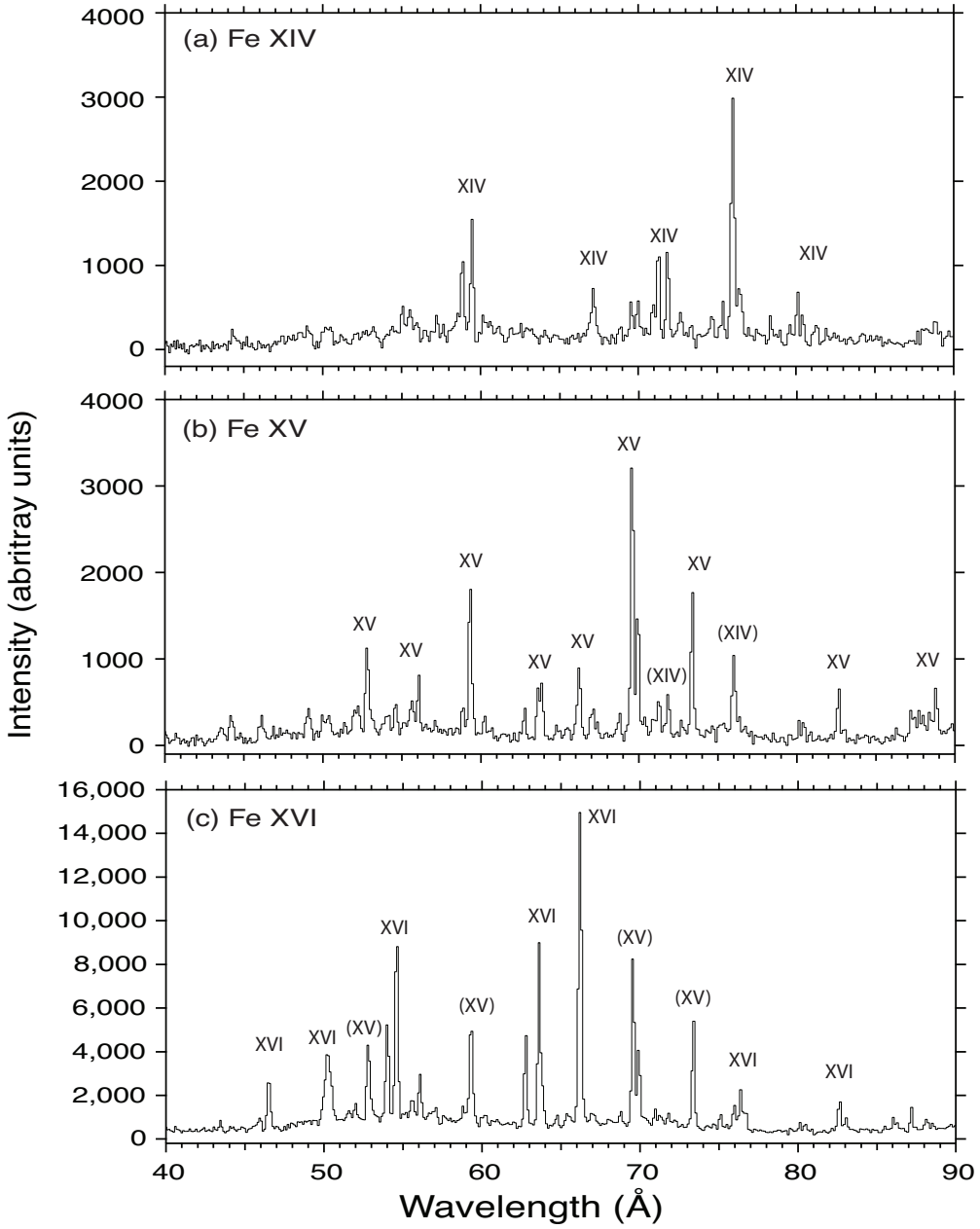

Fig. 1.— Iron spectra taken on the LLNL electron beam ion trap facility to illustrate the dominance of different charge states at different beam energies. (a) beam energy 360 eV: strongest lines belong to Fe XIV. (b) beam energy 420 eV: strongest lines belong to Fe XV.(c) beam energy 550 eV: strongest lines belong to Fe XVI. Select lines from Fe XIV and Fe XV are noted.

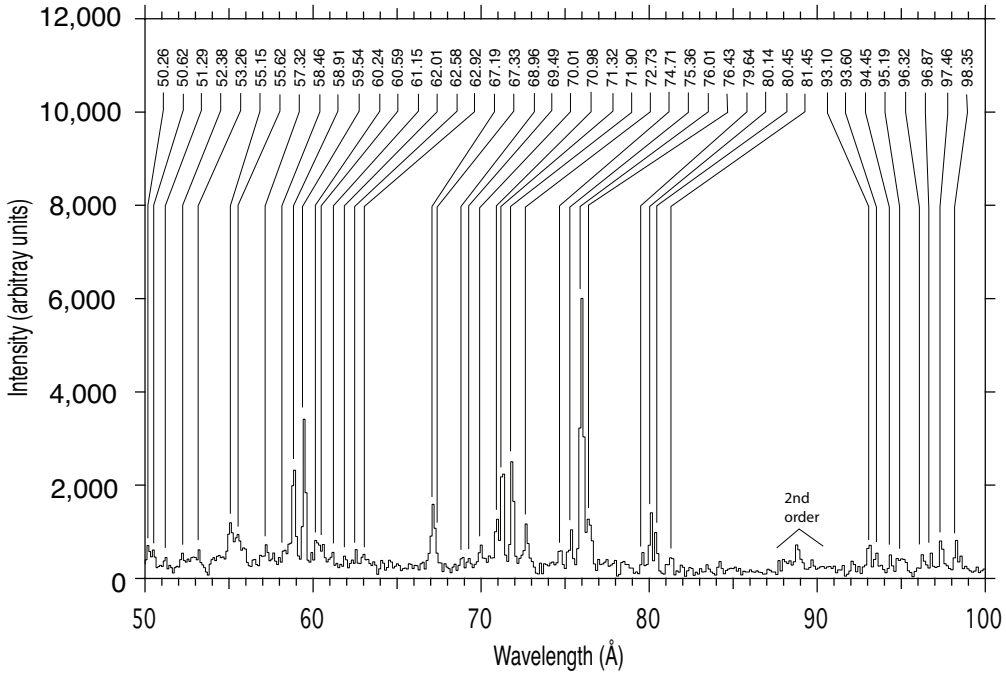

Fig. 2.— "Pure" spectrum of Fe XIV. See text for details of how other charge states were removed.

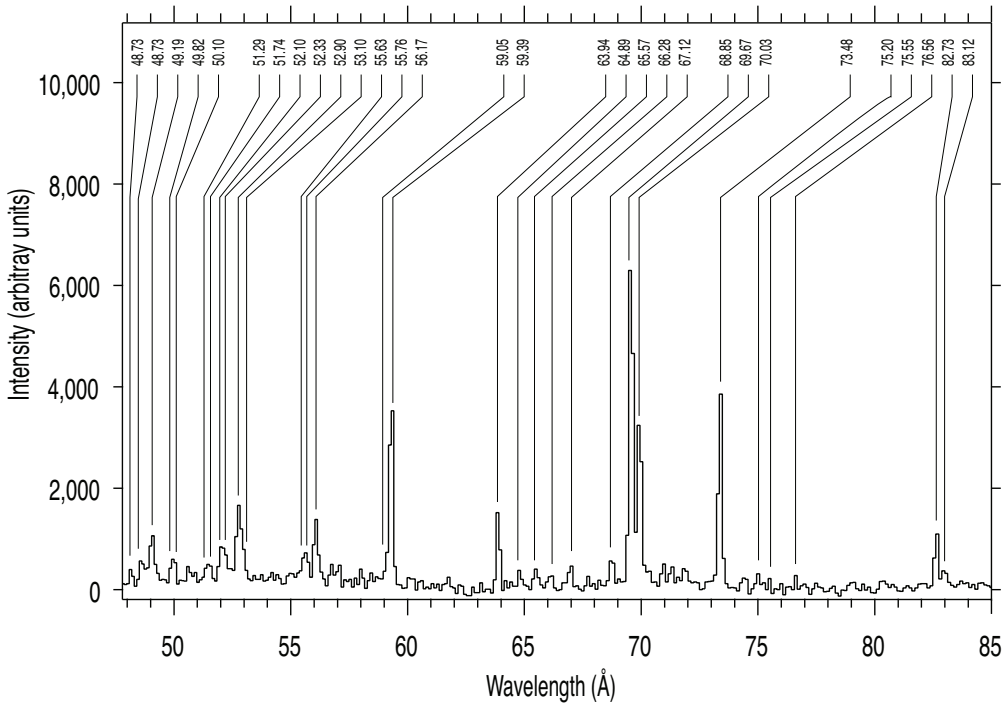

Fig. 3.— "Pure" spectrum of Fe XV. See text for details of how other charge states were removed.

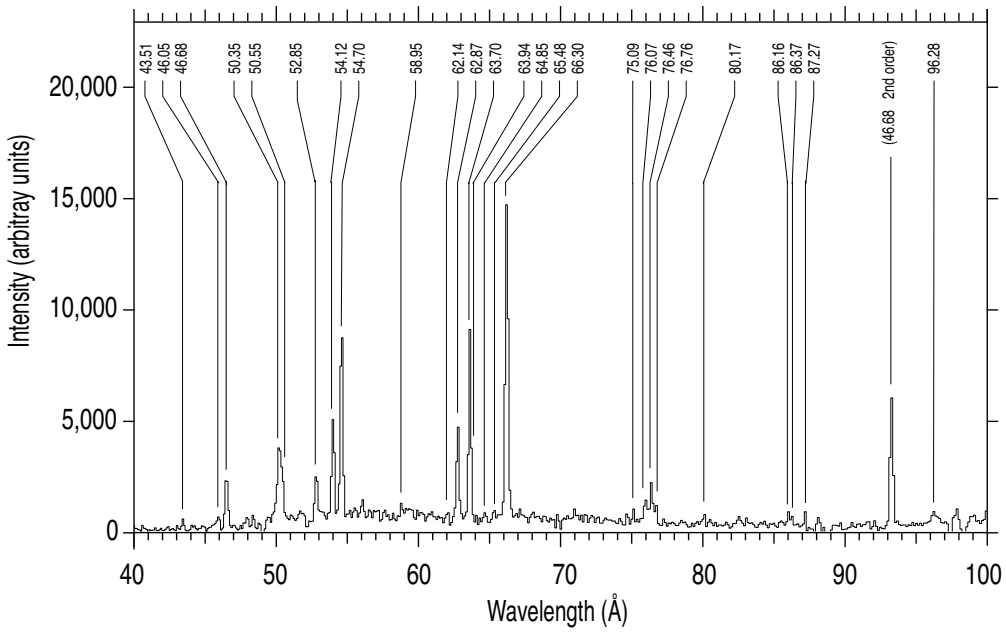

Fig. 4.— "Pure" spectrum of Fe XVI. See text for details of how other charge states were removed.

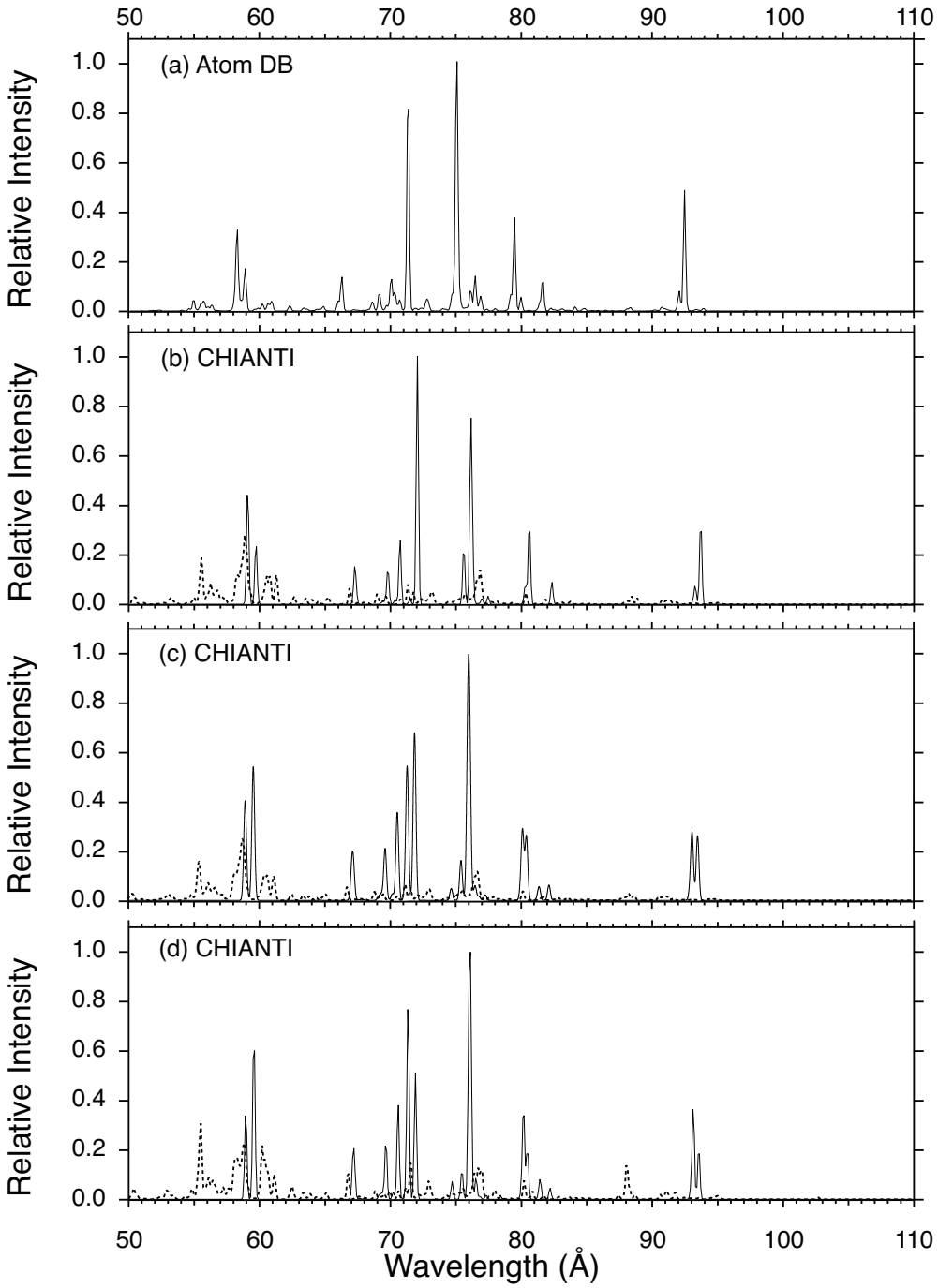

Fig. 5.— Comparison of Fe XIV spectra calculated at different densities and models. (a) Spectrum calculated with AtomDB at the zero-density limit; (b) CHIANTI spectrum calculated at 10^6 cm^{-3}; (c) CHIANTI spectrum calculated at 10^{10} cm^{-3}; (d) CHIANTI spectrum calculated at 10^{15} cm^{-3}. In the CHIANTI spectra, solid traces represent "verified", dotted traces represent "unverified" lines.

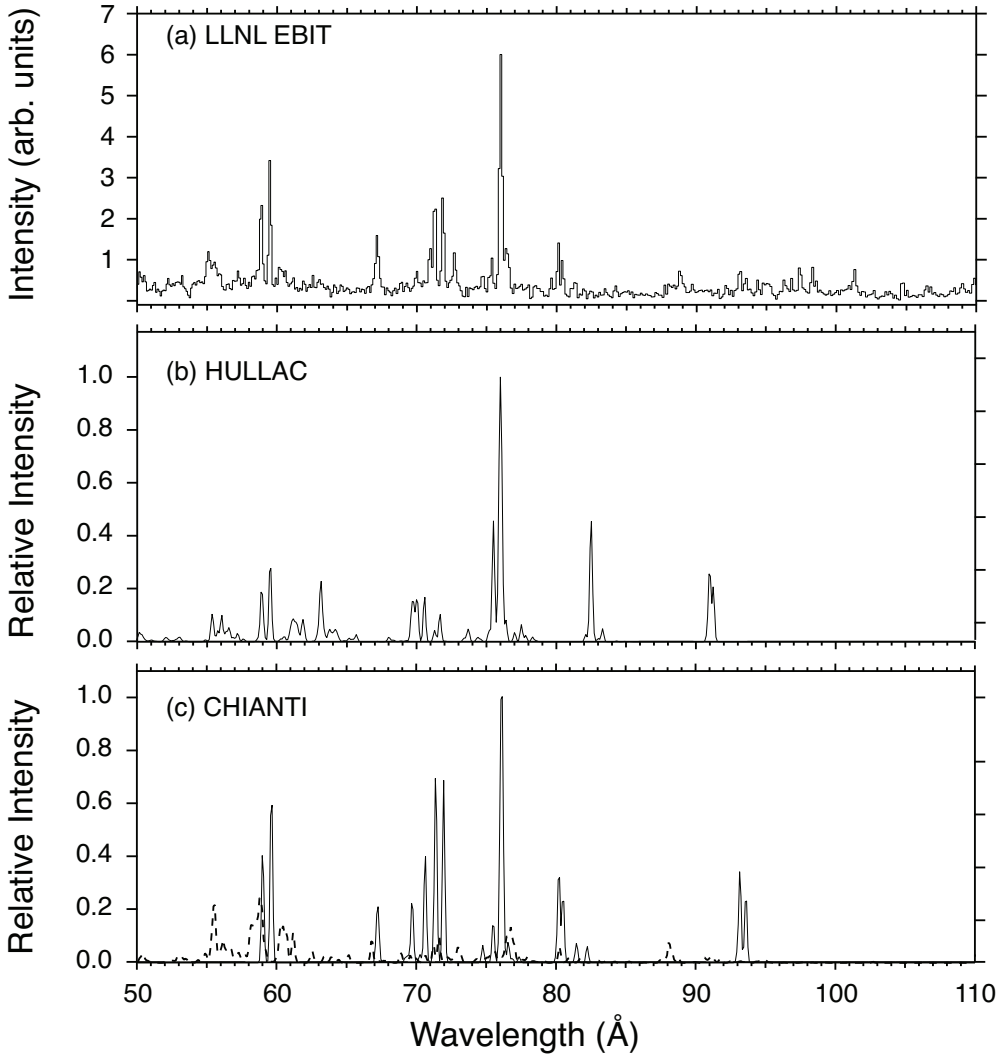

Fig. 6.— Comparison of measured and calculated Fe XIV spectra. (a) "Pure" spectrum from the Livermore EBIT recorded at a beam energy of 360 eV. (b) Synthetic spectrum derived from HULLAC calculations at a density of 5×10^{11} cm^{-3}. (c) Synthetic spectrum derived from the CHIANTI database at a density of 5×10^{12} cm^{-3}; solid lines are listed as "verified", while dotted lines are "unverified".

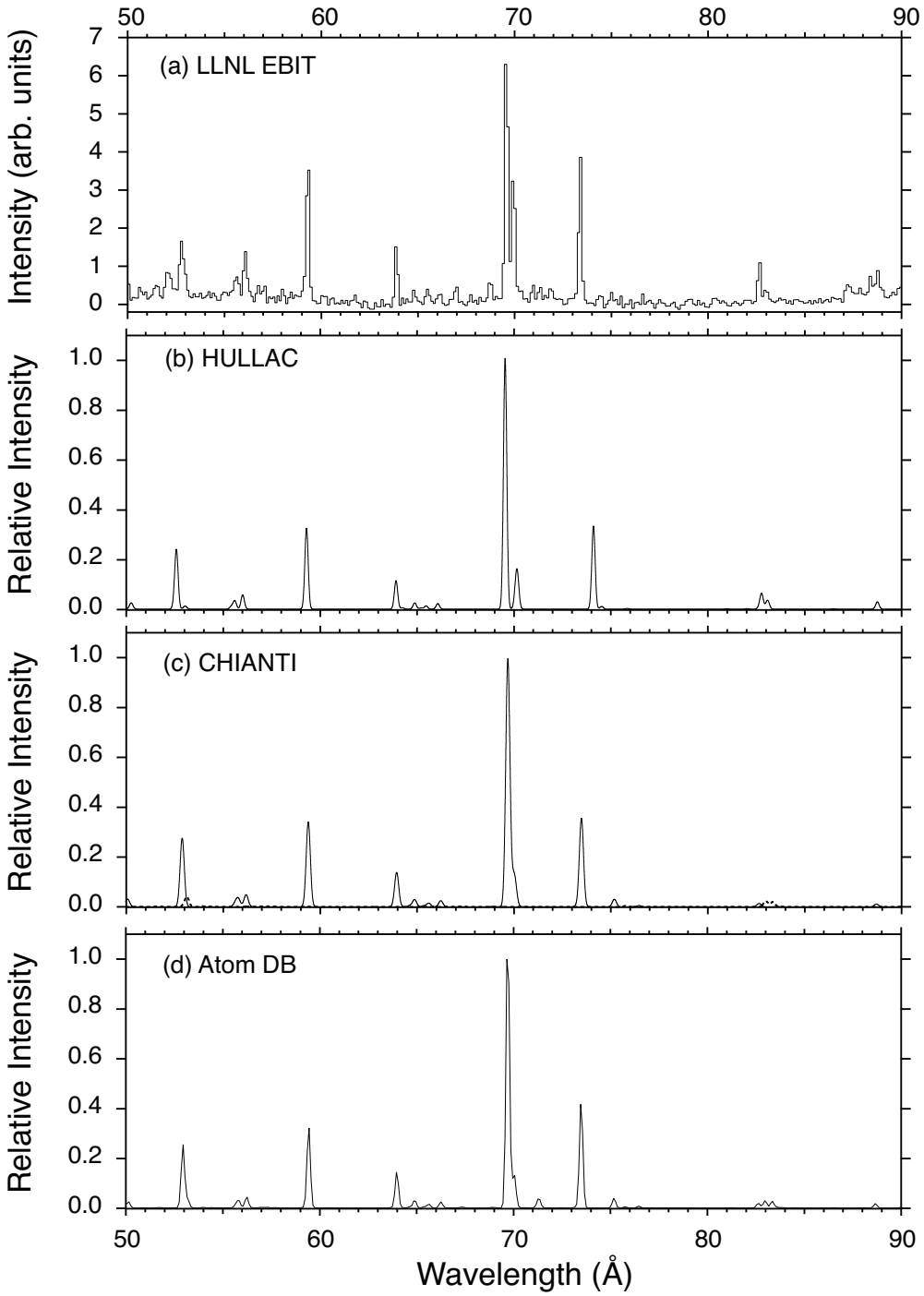

Fig. 7.— Comparison of measured and calculated Fe XV spectra. (a) "Pure" spectrum from the Livermore EBIT recorded at a beam energy of 420 eV. (b) Synthetic spectrum derived from HULLAC calculations at a density of 5×10^{11} cm^{-3}. (c) Synthetic spectrum derived from the CHIANTI database at a density of 1×10^{10} cm^{-3}; solid lines are listed as "verified", while dotted lines are "unverified". (d) Synthetic spectrum derived from the AtomDB database at the zero-density limit.

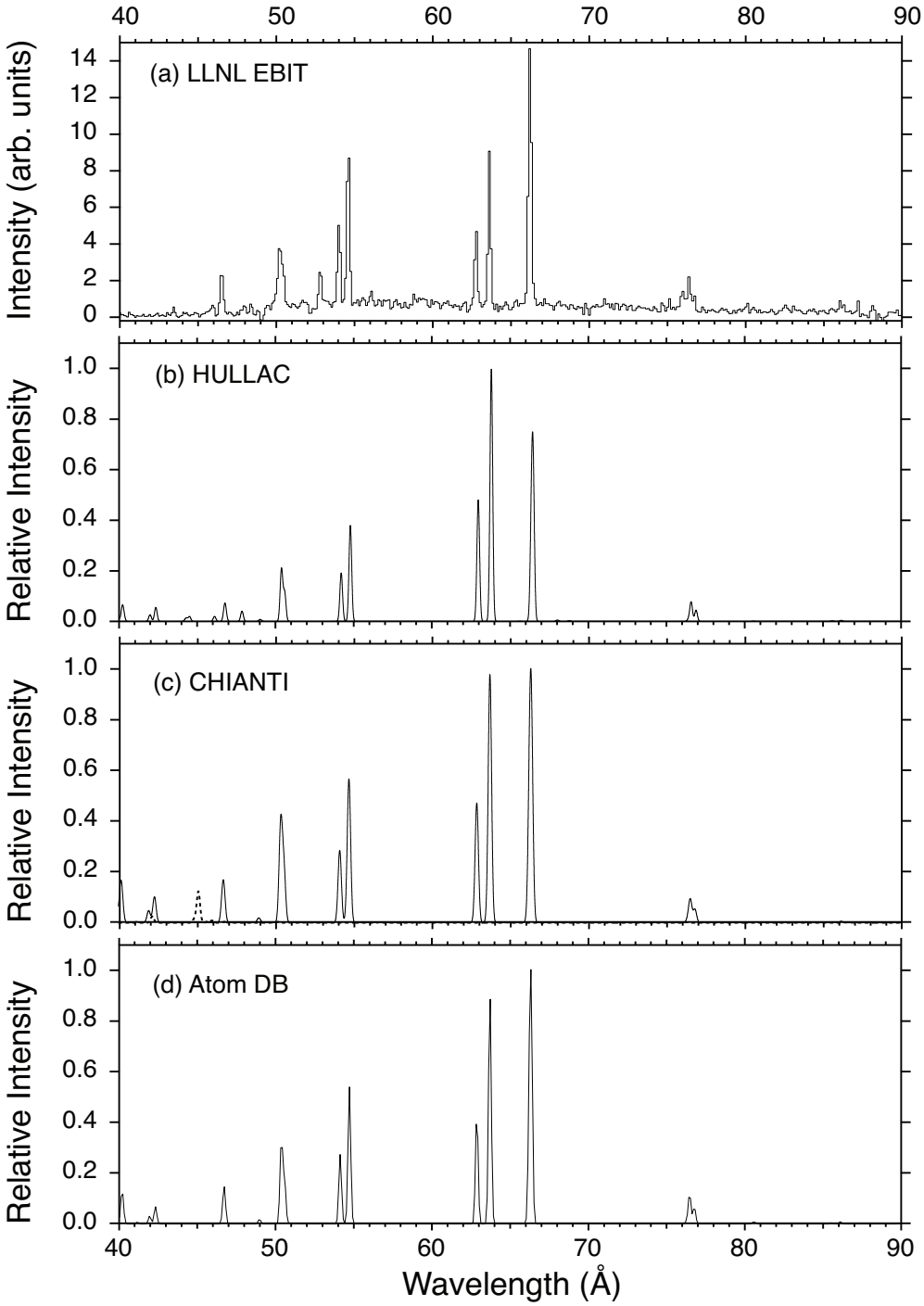

Fig. 8.— Comparison of measured and calculated Fe XVI spectra. (a) "Pure" spectrum from the Livermore EBIT recorded at a beam energy of 550 eV. (b) Synthetic spectrum derived from HULLAC calculations at a density of 5×10^{11} cm^{-3}. (c) Synthetic spectrum derived from the CHIANTI database at a density of 1×10^{10} cm^{-3}. Solid lines are listed as "verified", while dotted lines are "unverified". (d) Synthetic spectrum derived from the AtomDB database at the zero-density limit.

Table 1. Summary of iron emission lines for aluminum-like Fe XIV. We include experimental wavelength measurements with errors and intensities, plus wavelengths of lines included in the databases commonly used in astrophysics. Labelled features are those already found in the databases. We also include lines from calculations performed with HULLAC, listing line position, intensity, and the associated level configurations. Intensities are normalized on a scale of 1-20.

λ_{exp}	Standard Error$_{exp}$	I_{exp}	Kelly	SPEX	CHIANTI	λ_{HULLAC}	I_{HULLAC}	Upper Level	Lower Level
...	...	...	...	...	44.936 [a]	45.039	2	$(3s^2 5d)_{J=5/2}$	$(3s^2 3p)_{J=3/2}$
50.255	0.037	5	...	...	...	50.212	1	$(3s3p5s)_{J=3/2}$	$(3s3p^2)_{J=5/2}$
50.619	0.01	5	...	...	...	50.424	1	$(3s3p5s)_{J=1/2}$	$(3s3p^2)_{J=3/2}$
51.294	0.002	3	...	...	...	...	...	...	...
52.384	0.015	4	...	...	...	...	...	...	...
53.260	0.021	3	...	...	...	...	...	...	...
55.152	0.007	10	...	...	55.437 [a]	55.394	2	$(3s^2 5f)_{J=5/2}$	$(3s^2 3d)_{J=3/2}$
...	...	...	...	...	55.505 [a]	55.45	2	$(3s^2 5f)_{J=7/2}$	$(3s^2 3d)_{J=5/2}$
55.618	0.008	9	...	...	...	55.831	2	$(3s3p4p)_{J=3/2}$	$(3s^2 3p)_{J=1/2}$
...	...	...	...	...	55.559 [a]	56.107	3	$(3s3p4p)_{J=5/2}$	$(3s^2 3p)_{J=3/2}$
...	...	...	...	...	56.543 [a]	56.621	1	$(3s3p4p)_{J=1/2}$	$(3s^2 3p)_{J=1/2}$
57.316	0.006	5	...	...	56.963 [a]	57.273	1	$(3s3p4p)_{J=3/2}$	$(3s^2 3p)_{J=3/2}$
58.460	0.018	4	...	...	58.889 [a]	...	...	...	...
58.907	0.006	16	58.963	58.96	58.963	58.963	7	$(3s^2 4d)_{J=3/2}$	$(3s^2 3p)_{J=1/2}$
...	...	...	...	...	...	59.066	1	$(3s^2 5d)_{J=3/2}$	$(3s^2 3d)_{J=5/2}$
59.540	0.007	19	< 59.58 >	59.579	59.579	59.579	11	$(3s^2 4d)_{J=5/2}$	$(3s^2 3p)_{J=3/2}$
...	...	...	...	...	59.626	59.626	1	$(3s^2 4d)_{J=3/2}$	$(3s^2 3p)_{J=3/2}$
60.241	0.034	5	...	...	60.199 [a]	...	...	...	...
60.592	0.038	4	...	...	60.397 [a]	60.582	1	$(3s3p4d)_{J=5/2}$	$(3s3p^2)_{J=3/2}$
61.147	0.035	3	...	...	61.150 [a]	61.115	1	$(3s3p4d)_{J=5/2}$	$(3s3p^2)_{J=5/2}$
...	...	...	...	...	...	61.227	2	$(3s3p4d)_{J=5/2}$	$(3s3p^2)_{J=5/2}$
...	...	...	...	...	...	61.406	1	$(3s3p4d)_{J=7/2}$	$(3s3p^2)_{J=5/2}$
...	...	...	...	...	...	61.523	2	$(3s3p4d)_{J=5/2}$	$(3s3p^2)_{J=3/2}$
...	...	...	...	...	...	61.888	1	$(3s3p4d)_{J=7/2}$	$(3s3p^2)_{J=5/2}$
62.005	0.044	3	...	...	...	61.974	1	$(3s3p4d)_{J=5/2}$	$(3s3p^2)_{J=3/2}$
62.585	0.043	3	...	...	...	...	...	...	...
62.925	0.006	3	...	...	...	62.945	1	$(3s3p4d)_{J=1/2}$	$(3s3p^2)_{J=1/2}$
...	...	...	...	...	62.515 [a]	63.157	2	$(3s3p4d)_{J=3/2}$	$(3s3p^2)_{J=1/2}$
...	...	...	...	...	...	63.210	6	$(3s3p4d)_{J=7/2}$	$(3s3p^2)_{J=5/2}$
...	...	...	...	...	...	63.371	1	$(3s3p4d)_{J=5/2}$	$(3s3p^2)_{J=3/2}$
...	...	...	...	...	...	63.778	1	$(3s3p4d)_{J=5/2}$	$(3s3p^2)_{J=3/2}$
...	...	...	...	...	...	64.291	1	$(3s3p4d)_{J=5/2}$	$(3s3p^2)_{J=5/2}$
...	...	...	...	...	66.813 [a]	65.739	1	$(3s3p4d)_{J=5/2}$	$(3s3p^2)_{J=3/2}$
67.194	0.013	5 [b]	...	...	67.141	...	...	...	...
67.333	0.013	4 [b]	...	...	67.254	...	...	...	...
68.965	0.012	2	...	...	...	...	...	...	...
69.485	0.037	4	...	69.685	69.685	69.685	3	$(3s^2 4s)_{J=1/2}$	$(3s^2 3p)_{J=1/2}$
...	...	...	...	...	...	69.836	4	$(3s^2 4f)_{J=5/2}$	$(3s3p^2)_{J=3/2}$
...	...	...	...	...	...	69.989	1	$(3s3p4s)_{J=3/2}$	$(3s3p^2)_{J=5/2}$
70.012	0.006	4	...	...	...	70.096	5	$(3s^2 4f)_{J=7/2}$	$(3s3p^2)_{J=5/2}$
70.977	0.007	5	...	70.613	70.613	70.613	7	$(3s^2 4s)_{J=1/2}$	$(3s^2 3p)_{J=3/2}$
71.324	0.006	9	< 71.38 >	...	...	71.359	1	$(3s3p4s)_{J=1/2}$	$(3s3p^2)_{J=1/2}$
71.903	0.007	9	< 71.87 >	...	71.580 [a]	71.708	4	$(3s3p4s)_{J=3/2}$	$(3s3p^2)_{J=3/2}$
...	...	...	...	...	71.939	71.769	1	$(3s3p4s)_{J=1/2}$	$(3s3p^2)_{J=3/2}$
72.731	0.014	5	...	...	...	73.771	2	$(3s3p4s)_{J=5/2}$	$(3s3p^2)_{J=5/2}$
74.705	0.031	3	...	...	...	...	...	...	...
75.361	0.026	4	...	...	...	75.224	2	$(3s3p4s)_{J=3/2}$	$(3s3p^2)_{J=3/2}$
...	...	...	...	...	...	75.539	17	$(3s3p4s)_{J=3/2}$	$(3s3p^2)_{J=5/2}$
...	...	...	...	...	...	75.678	2	$(3s3p4s)_{J=3/2}$	$(3s3p^2)_{J=1/2}$

Table 1—Continued

λ_{exp}	Standard Error$_{exp}$	I_{exp}	Kelly	SPEX	CHIANTI	λ_{HULLAC}	I_{HULLAC}	Upper Level	Lower Level
...	...	...	...	76.152	76.151	76.124	20	$(3s^2 4f)_{J=7/2}$	$(3s^2 3d)_{J=5/2}$
...	...	...	...	...	...	76.136	1	$(3s^2 4f)_{J=5/2}$	$(3s^2 3d)_{J=5/2}$
76.428	0.028	6	...	...	77.015 [a]	...	...	...	...
...	...	...	...	...	...	76.435	3	$(3s3p4s)_{J=1/2}$	$(3s3p^2)_{J=1/2}$
...	...	...	...	...	...	76.767	1	$(3s3p4f)_{J=7/2}$	$(3s3p^2)_{J=5/2}$
...	...	...	...	...	76.570	77.067	1	$(3s3p4s)_{J=3/2}$	$(3s3p^2)_{J=1/2}$
...	...	...	...	...	...	77.545	2	$(3s3p4s)_{J=3/2}$	$(3s3p^2)_{J=3/2}$
...	...	...	...	...	...	...	...	...	...
...	...	...	...	...	...	...	...	...	...
...	...	...	...	...	80.206	...	...	...	...
79.639	0.038	2	...	...	...	82.149	1	$(3s^2 4p)_{J=3/2}$	$(3s3p^2)_{J=3/2}$
80.142	0.025	4	...	...	...	82.499	7	$(3s^2 4p)_{J=1/2}$	$(3s3p^2)_{J=3/2}$
80.453	0.028	3	...	...	80.503	82.525	10	$(3s^2 4p)_{J=3/2}$	$(3s3p^2)_{J=3/2}$
81.450	0.041	2	...	...	81.480	82.586	3	$(3s3p4s)_{J=3/2}$	$(3s^2 3d)_{J=5/2}$
...	...	...	...	...	...	83.350	2	$(3s3p4s)_{J=1/2}$	$(3s^2 3d)_{J=3/2}$
88.431	0.043	2	...	...	...	...	...	...	...
88.937	0.02	4	...	...	88.103 [a]	...	...	...	...
89.740	0.022	2	...	...	...	...	...	...	...
...	...	...	...	...	...	...	...	...	...
...	...	...	...	...	...	...	...	...	...
...	...	...	...	...	...	...	...	...	...
92.236	0.011	2	...	...	...	90.844	1	$(3s^2 4p)_{J=3/2}$	$(3s^2 3d)_{J=3/2}$
93.096	0.018	4	91.009	91.009	93.192	91.009	11	$(3s^2 4p)_{J=3/2}$	$(3s^2 3d)_{J=5/2}$
93.604	0.028	3	91.273	91.273	93.614	91.273	8	$(3s^2 4p)_{J=1/2}$	$(3s^2 3d)_{J=3/2}$
94.452	0.043	2	...	...	...	...	...	...	...
95.190	0.031	3	...	...	...	...	...	...	...
96.319	0.074	3	...	...	...	...	...	...	...
96.870	0.048	2	...	...	...	...	...	...	...
97.459	0.014	5	...	...	...	...	...	...	...
98.346	0.007	5	...	...	...	...	...	...	...

[a]isted as "unverified" in CHIANTI

Table 2. Summary of iron emission lines for magnesium-like Fe XV. We include experimental wavelength measurements with errors and intensities, plus wavelengths of lines included in the databases commonly used in astrophysics. Labelled features are those already found in the databases. We also include lines from calculations performed with HULLAC, listing line position, intensity, and the associated level configurations. Intensities are normalized on a scale of 1-20.

λ_{exp}	Standard Error$_{exp}$	I_{exp}	Kelly	SPEX	CHIANTI	λ_{HULLAC}	I_{HULLAC}	Upper Level	Lower Level
...	...	...	...	...	43.781[b] 43.772	1	$(3s5d)_{J=2}$	$(3s3p)_{J=1}$	
44.23	0.02	4[a]		...	...	...	...	...	...
...									
44.45	0.002	9[a]	...	...	...	...	...	...	...
44.99	0.014	4	...	...	...	...	...	...	...
46.14	0.005	5	...	...	46.287[b]	46.244	1	$(3s5s)_{J=0}$	$(3s3p)_{J=1}$
48.19	0.036	3	...	...	...	...	...	...	...
48.73	0.004	4	...	...	...	...	...	...	...
49.19	0.005	10	...	...	49.490	...	...	...	...
49.82	0.006	2[a]	...	...	...	...	...	...	...
50.10	0.003	5[a]	"< 50.06, 50.08, 50.12 >"	...	50.121	50.26	< 1	$(3s5f)_{J=4}$	$(3s3d)_{J=3}$
50.53	0.012	3	...	...	...	...	...	...	...
51.29	0.002	2[a]	...	...	...	...	...	...	...
51.74	0.015	3[a]	...	...	...	...	...	...	...
52.10	0.005	5	...	...	...	...	...	...	...
52.33	0.012	4	...	...	...	52.491	1	$(3s5f)_{J=3}$	$(3s3d)_{J=2}$
52.90	0.003	12[a]	52.91	52.911	52.911	...	...	...	...
53.10	0.006	6[a]	...	...	53.165[b]	52.577	4	$(3s4p)_{J=1}$	$(3s^2)_{J=0}$
55.63	0.011	4[a]	< 55.63 >	55.635	55.792	55.578	1	$(3s4d)_{J=2}$	$(3s3p)_{J=1}$
55.76	0.011	5[a]	...	55.793	56.200	55.991	1	$(3s4d)_{J=3}$	$(3s3p)_{J=2}$
56.17	0.003	9	< 56.20 >	56.200	...	...	...	...	...
56.81	0.021	3	...	...	...	...	...	...	...
57.16	0.014	3	...	...	...	...	...	...	...
58.17	0.011	2	...	...	...	...	...	...	...
59.05	0.037	2[a]	...	...	...	...	...	...	...
59.39	0.002	14[a]	...	59.404	59.405	59.289	7	$(3s4d)_{J=2}$	$(3s3p)_{J=1}$
59.57	0.002	5[a]	...	...	...	...	...	...	...
60.35	0.013	3	...	...	...	...	...	...	...
61.93	0.033	1	...	...	...	...	...	...	...
63.94	0.004	5	...	63.960	63.957	63.912	2	$(3s4f)_{J=3}$	$(3s3p)_{J=2}$
64.89	0.003	2	...	...	64.878	64.877	1	$(3s4f)_{J=3}$	$(3s3p)_{J=2}$
65.57	0.016	2	...	65.612	65.615	65.463	< 1	$(3s4s)_{J=1}$	$(3s3p)_{J=2}$
...	...	...	...	...	...	66.07	1	$(3s4s)_{J=0}$	$(3s3p)_{J=1}$
66.28	0.016	2	...	66.238	66.230	...	...	...	...
67.12	0.014	2	...	...	67.181[b]	...	...	...	...
67.64	0.117	1	...	...	...	...	...	...	...
68.85	0.005	2	...	...	...	...	...	...	...
69.67	0.003	20	< 69.66 >	69.660	69.682	69.545	20	$(3s4s)_{J=0}$	$(3s3p)_{J=1}$
70.03	0.004	10	"< 69.94, 69.98, 70.05 >"	"< 69.945, 69.987, 70.054 >"	69.941	70.083	1	$(3s4f)_{J=2}$	$(3s3d)_{J=1}$
...	...	...	...	...	69.987	70.124	1	$(3s4f)_{J=3}$	$(3s3d)_{J=2}$
...	...	...	...	...	70.054	70.189	2	$(3s4f)_{J=4}$	$(3s3d)_{J=3}$
71.05	0.011	2	< 71.06 >	...	...	...	...	...	...
71.36	0.01	2	...	...	...	...	...	...	...
71.94	0.009	2	...	...	...	...	...	...	...
73.48	0.003	9	< 73.41 >	73.471	73.472	74.107	7	$(3s4f)_{J=3}$	$(3s3d)_{J=2}$
74.53	0.048	1	...	...	...	...	...	...	...
75.20	0.017	1	...	...	75.167	74.528	< 1	$(3s4p)_{J=1}$	$(3s3p)_{J=2}$
75.55	0.064	1	...	...	...	...	...	...	...
76.56	0.049	3	...	...	...	...	...	...	...
82.73	0.007	3	...	...	...	82.794	1	$(3s4p)_{J=2}$	$(3s3d)_{J=3}$
83.12	0.011	1	...	...	...	83.089	< 1	$(3s4p)_{J=1}$	$(3s3d)_{J=2}$
...	...	...	...	...	...	83.131	< 1	$(3s4p)_{J=0}$	$(3s3d)_{J=1}$

Table 2—Continued

λ_{exp}	Standard Error$_{exp}$	I_{exp}	Kelly	SPEX	CHIANTI	λ_{HULLAC}	I_{HULLAC}	Upper Level	Lower Level
...	...	...	...	...	...	88.769	1	$(3s4p)_{J=2}$	$(3s3d)_{J=2}$

[a]Used 1st order spectrum to measure line intensity and 2nd order spectrum to distinguish closely separated features

[b]isted as "unverified" in CHIANTI

Table 3. Summary of iron emission lines for sodium-like Fe XVI. We include experimental wavelength measurements with errors and intensities, plus wavelengths of lines included in the databases commonly used in astrophysics. Labelled features are those already found in the databases. We also include lines from calculations performed with HULLAC, listing line position, intensity, and the associated level configurations. Intensities are normalized on a scale of 1-20.

λ_{exp}	Standard Error$_{exp}$	I_{exp}	Kelly	SPEX	CHIANTI	λ_{HULLAC}	I_{HULLAC}	Upper Level	Lower Level
...	...	...	...	...	39.8271	39.897	1	$(5d)_{J=3/2}$	$(3p)_{J=1/2}$
...	...	...	...	...	40.1531	40.22	1	$(5d)_{J=5/2}$	$(3p)_{J=3/2}$
...	...	...	...	...	41.9321	41.994	1	$(5s)_{J=1/2}$	$(3p)_{J=1/2}$
43.506	0.014	4	...	...	...	...	...	...	...
46.051	0.062	3	...	...	...	...	...	...	...
46.685	0.006	10	...	46.694	46.6614	46.761	1	$(5f)_{J=5/2}$	$(3d)_{J=3/2}$ 49.485
0.029	5	...	...	...	...	...	...	...	
50.077	0.012	5	...	...	...	...	...	...	...
50.355	0.004	16	50.35	50.350	50.3610	50.415	4	$(4p)_{J=3/2}$	$(3s)_{J=1/2}$
50.554	0.004	10	50.56	50.555	50.5650	50.623	2	$(4p)_{J=1/2}$	$(3s)_{J=1/2}$
51.153	0.051	2	...	...	...	...	...	...	...
51.7	0.012	4	...	...	...	...	...	...	...
52.851	0.02	9	...	...	...	...	...	...	...
53.095	0.008	4	...	...	...	...	...	...	...
54.115	0.004	12	...	54.142	54.1260	54.244	4	$(4d)_{J=3/2}$	$(3p)_{J=1/2}$
54.7	0.003	20	$< 54.72 >$	54.728	54.7100	54.826	7	$(4d)_{J=5/2}$	$(3p)_{J=3/2}$
...	...	...	...	54.769	54.7470	54.864	1	$(4d)_{J=3/2}$	$(3p)_{J=3/2}$
55.144	0.008	2	...	...	...	...	...	...	...
55.725	0.015	2	...	...	...	...	...	...	...
56.17	0.015	3	...	...	...	...	...	...	...
57.147	0.007	2	...	...	...	...	...	...	...
57.758	0.069	2	...	...	...	...	...	...	...
58.947	0.015	3	...	...	...	...	...	...	...
58.947	0.015	3	...	...	...	...	...	...	...
60.073	0.034	1	...	...	...	...	...	...	...
60.332	0.012	1	...	...	...	...	...	...	...
62.136	0.038	2	...	...	...	...	...	...	...
62.872	0.005	7	$< 62.88 >$	62.879	62.8710	63.025	10	$(4s)_{J=1/2}$	$(3p)_{J=1/2}$
63.699	0.002	13	$< 63.72 >$	63.719	63.7110	63.864	20	$(4s)_{J=1/2}$	$(3p)_{J=3/2}$
63.941	0.011	1	...	...	...	...	...	...	...
64.852	0.019	2	...	...	...	...	...	...	...
65.481	0.009	2	...	...	...	...	...	...	...
66.299	0.006	19	"$< 66.26, 66.37 >$"	66.326	66.2490	66.439	7	$(4f)_{J=5/2}$	$(3d)_{J=3/2}$
...	...	...	...	...	66.3570	66.541	10	$(4f)_{J=7/2}$	$(3d)_{J=5/2}$
...	...	...	...	...	66.3770	66.562	1	$(4f)_{J=5/2}$	$(3d)_{J=5/2}$
67.087	0.018	2	...	...	...	...	...	...	...
68.224	0.015	1	...	...	...	...	...	...	...
71.003	0.021	1	...	...	...	...	...	...	...
74.296	0.035	1	...	...	...	...	...	...	...
74.763	0.025	1	...	...	...	...	...	...	...
75.093	0.018	1	...	...	...	...	...	...	...
76.069	0.016	1	...	...	...	...	...	...	...
76.46	0.005	2	$< 76.50 >$	76.502	76.497	76.6660	2	$(4p)_{J=3/2}$	$(3d)_{J=5/2}$
76.756	0.005	1	$< 76.80 >$	76.796	76.796	76.9810	1	$(4p)_{J=1/2}$	$(3d)_{J=3/2}$
80.165	0.029	1	...	...	...	...	...	...	...
80.552	0.021	1	...	...	...	...	...	...	...
82.719	0.016	1	...	...	...	...	...	...	...
83.123	0.017	1	...	...	...	...	...	...	...
86.164	0.02	1	...	...	...	...	...	...	...
86.366	0.032	1	...	...	...	...	...	...	...
87.266	0.013	1	...	...	...	...	...	...	...